Charge-Transfer Interfaces

Deutsche Ausgabe: DOI: 10.1002/ange.201605247
Internationale Ausgabe: DOI: 10.1002/anie.201605247

Dual Oxygen and Tungsten Vacancies on a WO_3 Photoanode for Enhanced Water Oxidation

Ming Ma[+], Kan Zhang[+], Ping Li, Myung Sun Jung, Myung Jin Jeong, and Jong Hyeok Park*

Abstract: *Alleviating charge recombination at the electrode/electrolyte interface by introducing an overlayer is considered an efficient approach to improve photoelectrochemical (PEC) water oxidation. A WO_3 overlayer with dual oxygen and tungsten vacancies was prepared by using a solution-based reducing agent, LEDA (lithium dissolved in ethylenediamine), which improved the PEC performance of the mesoporous WO_3 photoanode dramatically. In comparison to the pristine samples, the interconnected WO_3 nanoparticles surrounded by a 2–2.5 nm thick overlayer exhibited a photocurrent density approximately 2.4 times higher and a marked cathodic shift of the onset potential, which is mainly attributed to the facilitative effect on interface charge transfer and the improved conductivity by enhanced charge carrier density. This simple and effective strategy may provide a new path to improve the PEC performance of other photoanodes.*

PEC water splitting has become a central research theme for more than four decades.[1,2] However, the efficiency of PEC water splitting materials still remains low. Despite extensive efforts devoted to modifying photoelectrodes by various band gap and catalysis engineering strategies, efficient methods for charge transfer at the electrode/electrolyte interface remain underdeveloped. Especially for photoanodes, the highly oxidizing valence band (VB) holes need to be delivered to the anode surface, where charge recombination or back-reaction substantially limits water oxidation.[3] Thus, efficient charge transfer across the electrode/electrolyte interface is critical for achieving high solar energy conversion efficiency.

To date, overcoating is regarded as the most promising strategy to improve interfacial charge transfer, which promotes minority carrier migration and is substantially dependent on a lattice matched interface.[4,5] For example, an epitaxially grown rutile TiO_2 overlayer on rutile TiO_2 wires exhibited a 1.5-fold enhanced PEC performance, whereas the same performance was not obtained with an anatase TiO_2 overlayer.[6] Ji et al. grew a $SrTiO_3$ overlayer epitaxially on a Si(001) photocathode, achieving a 35 mA cm^{-2} photocurrent density.[7] The nearly defect-free interfaces achieved in such cases minimize ohmic loss levels, thereby facilitating interface charge transfer. However, the approach of pairing two lattice-matched materials is severely limited, and the epitaxial growth process largely depends on elaborate designs and complex components.

Recently, simple deposition of an amorphous TiO_2 overlayer on a series of photoanodes has been reported to serve as a hole-trapping layer to mitigate interfacial recombination.[8,9] A ferroelectric $BaTiO_3$ overlayer on TiO_2 photoanodes promotes interface charge transfer by the ferroelectric or piezoelectric effect.[10] From the perspective of charge polarization, outward driving forces (such as hole trapping and ferroelectric or piezoelectric potential) may drive highly oxidizing VB hole migration, thus alleviating energy loss at the intrinsic potential barrier at the photoanode/electrolyte interface. In this regard, vacancies (an important class of dopant) could also act as electron or hole acceptors with an influence on charge recombination.[11,12] However, conventional vacancies in the bulk region diminish the electron mobility to some extent because of their state localization. Therefore, modulating the functions of vacancies using

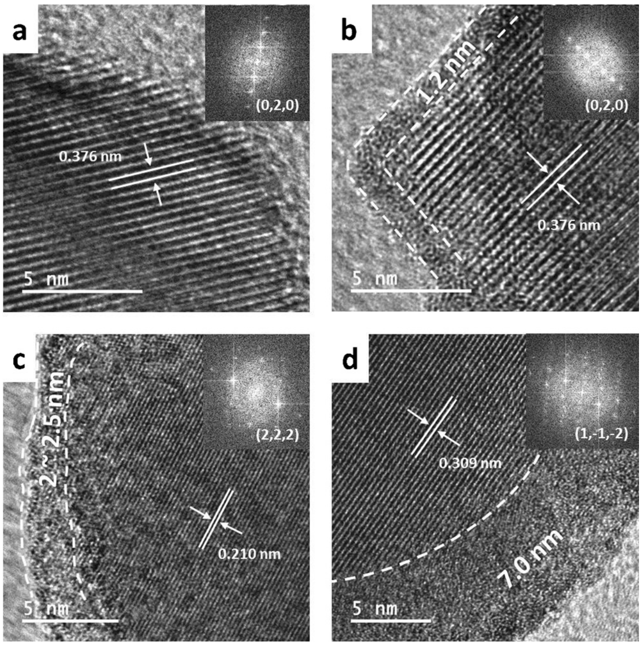

Figure 1. HRTEM images of WO_3 with treatment times of a) 0 s, b) 10 s, c) 20 s, and d) 40 s. The insets show fast Fourier transform diffraction patterns of the crystallographic parts.

---

[*] M. Ma,[+] Dr. K. Zhang,[+] P. Li, M. S. Jung, M. J. Jeong, Prof. J. H. Park
Department of Chemical and Biomolecular Engineering
Yonsei University
Seoul 120-749 (Republic of Korea)
E-mail: lutts@yonsei.ac.kr

M. Ma,[+] P. Li
SKKU Advanced Institute of Nano Technology
Sungkyunkwan University
Suwon 440-746 (Republic of Korea)

[+] These authors contributed equally to this work.

Supporting information for this article can be found under: http://dx.doi.org/10.1002/anie.201605247.

a finely controlled synthetic method is important for achieving charge polarization in a PEC electrode.[13,14]

Herein, we report a mesoporous WO_3 photoanode with a dual vacancy-containing overlayer, which was prepared from a solution state LEDA reagent. The overlayer significantly increases charge carrier density and induces a gradient band structure that helps charge transfer at the electrode/electrolyte interface. A 2–2.5 nm thick overlayer significantly promoted interface charge transfer efficiency from an initial 39 % to 90 % at 1.23 V (vs. RHE), as evidenced by a markedly negative shift of the onset potential and a dramatically enhanced photocurrent density.

Uniformly sized WO_3 films were prepared according to a previously reported method.[15] The thicknesses of the WO_3 films were controlled with the number of deposition layers, ranging from one to five (Supporting Information, Figure S1). A liquid reducing agent (LEDA) with a suitable concentration was used to treat the WO_3 films for up to 40 s (Supporting Information, Figure S2).[16] The morphologies of the WO_3 samples before and after treatment were investigated by scanning electron microscopy (SEM; Supporting Information, Figures S3 and S4). Neither the thickness nor the macroscopic surface structure of these films was altered. The shape and size of the WO_3 particles were further characterized with transmission electron microscopy (TEM), showing negligible change in the TEM images (Supporting Information, Figure S5). However, high resolution TEM (HRTEM) images of the treated WO_3 nanoparticles clearly showed an amorphous layer, which was detected on the basis of lattice disappearance (Figure 1). The thickness of the amorphous layer gradually increased with increasing LEDA treatment time and reached 7 nm after 40 s. The crystalline structure of WO_3 was indexed as the monoclinic phase (JCPDS No. 14-0688) from the XRD patterns (Supporting Information, Figure S6).[17,18] No changes were evident in the XRD patterns, thus indicating that the amorphous layer did not influence the original crystallinity. The light absorption behaviors were also recorded (Supporting Information, Figure S7 a), showing no adverse effect from the amorphous layer; the extracted band gap values of about 2.7 eV were approximately maintained (Supporting Information, Figure S7 b).

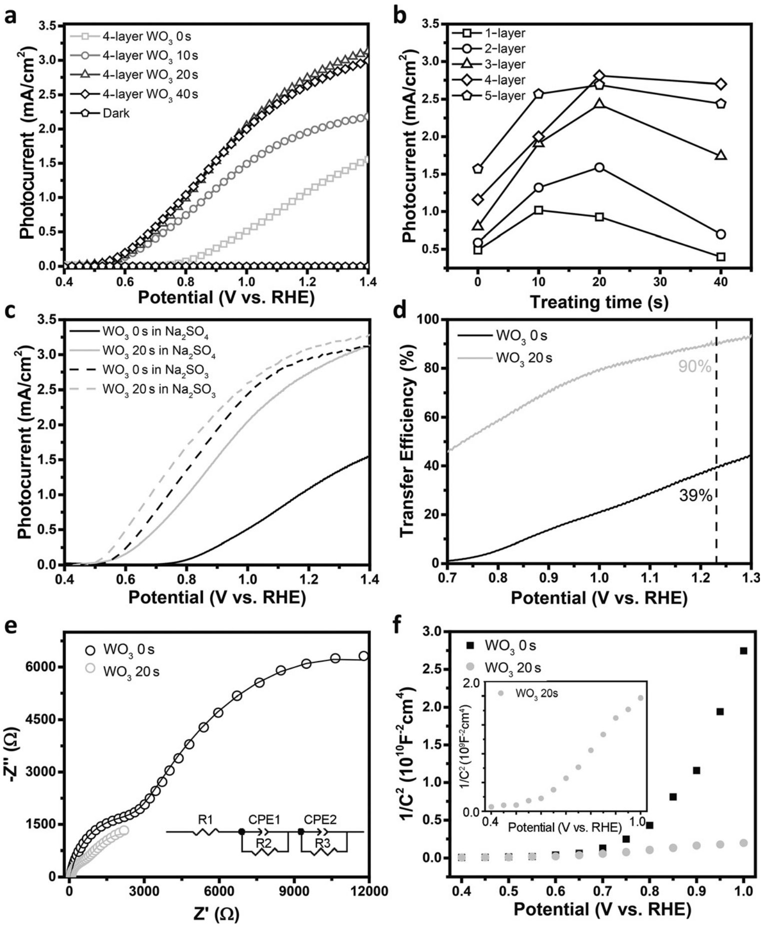

Figure 2. a) *J–V* curves of the four-layered WO_3 treated with LEDA over various periods, which were conducted in 0.5 M Na_2SO_4 electrolyte (ca. pH 6.8). b) Summary of photocurrent values at 1.23 V vs. RHE for all the samples (one to five layers). c) Photocurrent densities of WO_3 with treatment times of 0 s and 20 s, in 0.5 M Na_2SO_4 and 0.5 M Na_2SO_3 (pH buffered to ca. 7.5) electrolyte. d) Interface charge transfer efficiency and e) Nyquist plots with fitting curves of an equivalent circuit model (inset schematic) collected at 1.23 V vs. RHE for the 0 s and 20 s treated WO_3 samples. f) Comparison of the Mott–Schottky plots for the 0 s and 20 s treated WO_3 samples. The inset is the amplified graph of the 20 s treated sample.

Figure 2 a shows photocurrent density–potential (*J–V*) curves for four-layered WO_3 with various LEDA treatment times. The results clearly show that all of the treated samples exhibit markedly negative shifts of the onset potential, approximately 0.2 V, which is attributed to enhanced charge transfer.[19] The highest photocurrent density was obtained from the four-layer WO_3 treated for 20 s with an amorphous layer approximately 2–2.5 nm thick (Figure 1), and the value is about 2.81 $mA\,cm^{-2}$ at 1.23 V (vs. RHE), which is approximately 2.4 times greater than that of the untreated sample (Figure 2 a). Interestingly, when the treatment time was increased to 40 s, the photocurrent density exhibited a slight decrease, which might be due to the negative effects resulting from the thicker overlayer.[20] The fluctuation of photocurrent density as a function of treatment time exhibited the same tendency, regardless of the thickness of the WO_3 films (Supporting Information, Figure S8). This feature demonstrates that the enhanced PEC performances independently rely on the thickness of the amorphous layer upon the unit of WO_3 nanoparticles.

The values of photocurrent density of all the samples at 1.23 V (vs. RHE) are summarized in Figure 2 b, which depicts the influence of the amorphous layer on PEC performance, as well as the best conditions for LEDA treatment (as shown in Figure 2 a). Additionally, the WO_3 treated with pure ethylenediamine (EDA) solvent was also prepared as a control group (Supporting Information, Figure S9), which clearly illustrated no significant influence on PEC characteristics. PEC stabilities of WO_3 in a pristine state and after treatment for 20 s were also measured for more than 10 hours at 1.23 V (vs. RHE; Supporting Information, Figure S10). The WO_3 photoanodes with a dual-vacancy overlayer showed much improved water oxidation stability (ca. 73 % retention) compared to the pristine WO_3 (ca. 23 % retention). The photocurrent fading of the pristine WO_3 can be ascribed to the formation of peroxide species by hole accumulation during water oxidation in a Na_2SO_4 electrolyte, which leads to poisoning of WO_3.[21] The dual-vacancy overlayer efficiently passivates the WO_3 surface by fast hole transport, hence improving its stability. Enhanced charge transfer was quantified using a fast hole scavenger as the electrolyte, in this case Na_2SO_3 solution. The obtained *J–V* curves are shown in Figure 2 c, as a dashed line for Na_2SO_3 and a solid line for normal Na_2SO_4. The PEC performance of the best treated WO_3 photoanode, measured in Na_2SO_4, was approximately at the same extent as that for the untreated WO_3 measured in Na_2SO_3. Moreover, the negative shift of the onset potential and the photocurrent density of the treated WO_3 photoanodes were further enhanced when measured in Na_2SO_3. The amorphous layer remarkably improved charge transfer efficiency from 39 to 90 % at 1.23 V (vs. RHE; Figure 2 d), illustrating the facilitated water oxidation kinetics.[22] Assuming 100 % charge transfer efficiency in the presence of Na_2SO_3 hole scavenger, the superior PEC performance of the treated WO_3, with respect to that of untreated WO_3, illustrates the intrinsic difference between the amorphous overlayer and conventional overlayers.[5]

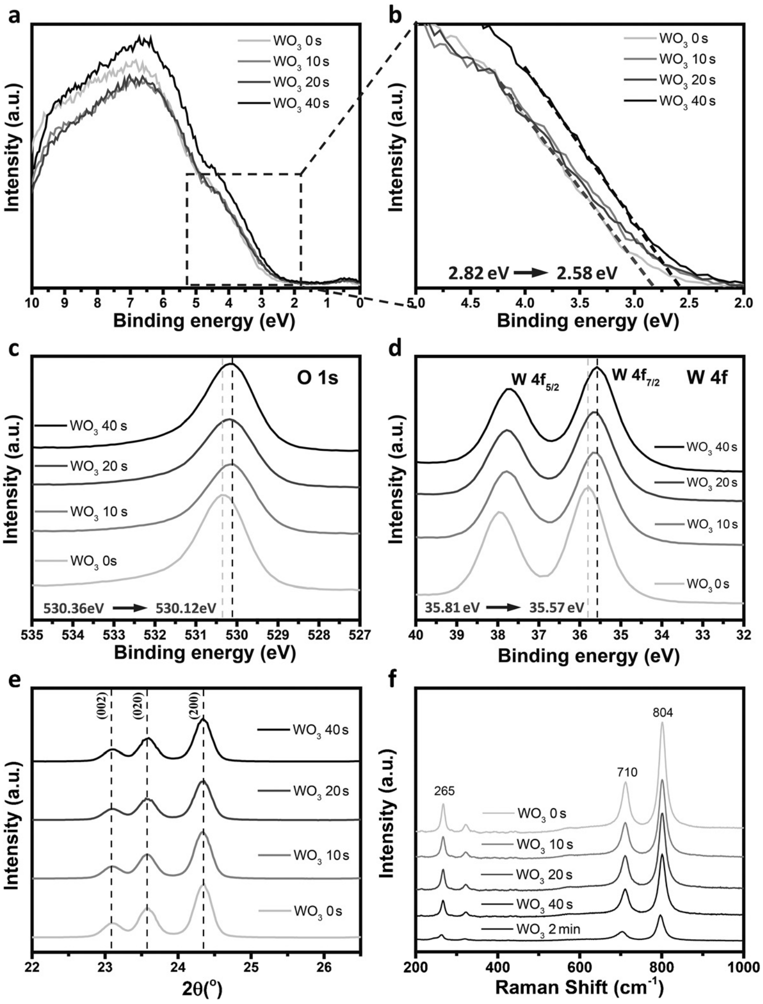

Figure 3. a) Valence band XPS spectra and b) the amplified selected section of WO_3 samples treated for 0 s, 10 s, 20 s, and 40 s. c) O 1s and d) W 4f XPS spectra of these samples. e) Selected section of the XRD spectra and f) Raman spectra.

According to the Nyquist plots and the fitting results (Figure 2 e; Supporting Information, Table S1), the treated WO_3 photoanodes exhibited remarkably decreased resistances in both charge transport and transfer processes when compared to pristine WO_3, illustrating the enhanced conductivity and facilitated interface charge transfer (see details in the Supporting Information and Table S1).[23] The Mott–Schottky plots in Figure 2 f show a markedly lower slope for the treated WO_3 photoanode. As the slopes of the plots are inversely proportional to the charge carrier densities,[24] the amorphous layer is responsible for the improved charge carrier density. Moreover, the flat band potential of the treated WO_3 exhibited a negative shift of approximately 0.2 V, which was associated with the cathodic shift of the onset potential measured in the case of the hole-scavenger electrolyte (Figure 2 c).[25,26]

X-ray photoelectron spectroscopy (XPS) was used to examine the surface chemical state. In the VB XPS data (Figure 3 a,b), the band positions showed an orderly cathodic shift as the treatment time increased from 0 s to 40 s, suggesting an upward VB position with a largest shift value of about 0.24 eV. The shifting phenomena were also observed in the O 1s and W 4f XPS spectra (Figure 3 c,d) with largest shift values of about 0.24 eV. The valence band shift can also be maintained in the electrolyte, as measured by electrochemical methods (Supporting Information, Figure S11). By combining these results with the shifted flat band potential and the maintained band gap values, we constructed a qualitative energy level diagram to characterize the influence of the amorphous layer on the surface properties (Supporting Information, Figure S12). The shifted band edges of the amorphous layer may be one reason for the enhanced charge transfer efficiency because the band edge gradient may drive migration of the hole.[27] Additionally, the entire survey and Li 1s XPS spectra were investigated to eliminate other contaminations, especially the lithium dopant (Supporting Information, Figure S13).

Previous chemical state modifications of WO_3, using various reduction methods,[28–30] have re-introduced H_xWO_3 and/or WO_{3-x} (W^{5+} or oxygen vacancies) components. Similarly, the amorphous layer formed by the reductive LEDA is assumed to contain H_xWO_3 and/or WO_{3-x}. In general, the formation of the H_xWO_3 species causes distortion and expansion of the lattice of the WO_3 crystal structure by atom intercalation, thus resulting in a shift of the diffraction peaks, (002), (020), and (200), in the XRD pattern.[31,32] However, no such shifting was observed in our case (Figure 3e); presumably H_xWO_3 did not form. Moreover, this assumption was further supported by the overlapped XPS O 1s spectra (Supporting Information, Figure S14a), which lacks a hydroxy peak and a broad shoulder at approximately 532 eV.[31] The presence of a WO_{3-x} component was indicated by the presence of W^{5+}. That is, the W 4f XPS peak of WO_{3-x} can be deconvoluted into two typical pairs of tungsten oxidation states: W^{6+} (centered at 37.7 and 35.5 eV) and W^{5+} (centered at 37.0 and 34.3 eV).[28,30] However, the W 4f XPS peak of our treated WO_3 could not be well deconvoluted into these two pairs. Moreover, the absence of the broad shoulder in the lower binding energy region about 34 eV also indicates that no obvious W^{5+} (oxygen vacancies) species were present in the amorphous layer (Supporting Information, Figure S14b).

To elucidate the real formation mechanism of the overlayer, we collected Raman spectra to reveal the surface bond energy states (Figure 3 f). After treatment with LEDA, the Raman intensities for both the W-O-W stretching (804 and 710 cm^{-1}) and bending (265 cm^{-1}) modes gradually decreased with increasing treatment time, clearly implying that changes occurred in the electronic energy level of the W-O-W bonds.[31,32] The result is in agreement with their Fourier transform infrared (FTIR) spectra (Supporting Information, Figure S15).

According to all of the aforementioned analyses, one hypothesis is that the amorphous layer is a consequence of oxygen and tungsten dual vacancies, which can be expressed as $W_{1-x}O_{3-y}$. We measured the ratios of oxygen and tungsten atoms at the surface of the WO_3 samples treated over different time spans to quantify the absence of oxygen and tungsten atoms (Supporting Information, Table S2). After LEDA treatment the O:W ratio decreased, which was coincident with improved carrier density and decreased Raman intensity. However, the ratios did not decrease with increasing treatment time, thus illustrating the simultaneous occurrence of tungsten and oxygen vacancies, resulting in a disordered lattice. As shown in Figure 4a, pristine WO_3 displayed continuous lattice fringes, associated with a normalized electronic structure. In contrast, the dual vacancy in WO_3 not only resulted in tungsten and oxygen atomic deficiencies but also affected the linear atomic arrangement in the ordered WO_3 lattice (Figure 4b), which may result in the enhanced charge carrier density, as observed from the Mott–Schottky plot. The presence of tungsten and oxygen vacancies was emphasized by high-angle annular dark-field (HAADF) images (Figure 4c,d). Interestingly, when the treated WO_3 was annealed under air to induce atomic rearrangement, the enhanced PEC performance accordingly disappeared (Figure 4e). This result suggests that the local electronic structure of WO_3 might be tailored to the dual-vacancy overlayer, which is responsible for enhanced water oxidation.

In summary, a WO_3 overlayer with dual oxygen and tungsten vacancies was formed by a facile solution-based process and exhibited beneficial behaviors that substantially enhanced the PEC water oxidation of the mesoporous WO_3 photoanode by dramatically improving the charge transfer efficiency, as evidenced by a cathodic shift of the onset potential. Moreover, the well-defined WO_3 overlayer with dual tungsten and oxygen vacancies also influenced the local electronic structure of WO_3 at the atomic scale, thereby increasing the charge carrier density of the WO_3 photoanode.

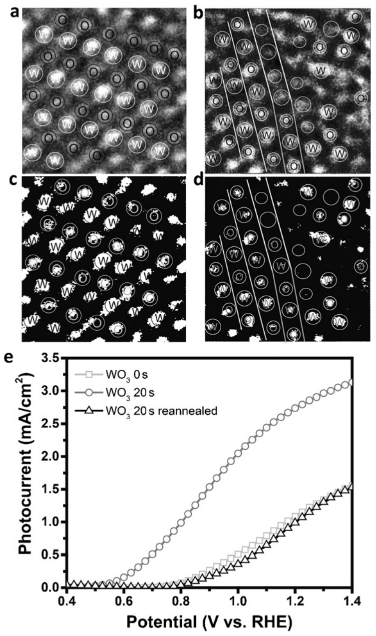

Figure 4. HRTEM images at the atomic scale of a) pristine and b) dual vacancy WO_3. HAADF images of c) pristine and d) dual vacancy WO_3. e) Photocurrent densities of WO_3 in pristine, dual vacancy, and reannealed dual vacancy forms.

Acknowledgements

This work was supported in part by the Yonsei University Future-leading Research Initiative of 2015(2015-22-0067). This work was partially supported by the NRF of Korea Grant funded by the Ministry of Science, ICT and Future Planning (NRF-2013R1A2A1A09014038, 2015M1A2A2074663, 2016M3D3A1A01913117 (C1 Gas Refinery Program)).

Keywords: amorphous overlayers · dual vacancy · photoelectrochemical · water oxidation · WO_3

How to cite: *Angew. Chem. Int. Ed.* **2016**, *55*, 11819–11823
Angew. Chem. **2016**, *128*, 11998–12002

[1] A. Fujishima, K. Honda, *Nature* **1972**, *238*, 37–38.
[2] D. G. Nocera, *Acc. Chem. Res.* **2012**, *45*, 767–776.
[3] F. E. Osterloh, *Chem. Soc. Rev.* **2013**, *42*, 2294–2320.
[4] Q. Yu, X. Meng, T. Wang, P. Li, J. Ye, *Adv. Funct. Mater.* **2015**, *25*, 2686–2692.
[5] T. W. Kim, K. Choi, *Science* **2014**, *343*, 990–994.
[6] Y. J. Hwang, C. Hahn, B. Liu, P. Yang, *ACS Nano* **2012**, *6*, 5060–5069.
[7] L. Ji, M. D. McDaniel, S. Wang, A. B. Posadas, X. Li, H. Huang, J. C. Lee, A. A. Demkov, A. J. Bard, J. G. Ekerdt, E. T. Yu, *Nat. Nanotechnol.* **2015**, *10*, 84–90.

[8] S. Hu, M. R. Shaner, J. A. Beardslee, M. Lichterman, B. S. Brunschwig, N. S. Lewis, *Science* **2014**, *344*, 1005 – 1009.

[9] D. Eisenberg, H. S. Ahn, A. J. Bard, *J. Am. Chem. Soc.* **2014**, *136*, 14011 – 14014.

[10] W. Yang, Y. Yu, M. B. Starr, X. Yin, Z. Li, A. Kvit, S. Wang, P. Zhao, X. Wang, *Nano Lett.* **2015**, *15*, 7574 – 7580.

[11] J. Deng, X. Lv, J. Gao, A. Pu, M. Li, X. Sun, J. Zhong, *Energy Environ. Sci.* **2013**, *6*, 1965 – 1970.

[12] F. Lei, Y. Sun, K. Liu, S. Gao, L. Liang, B. Pan, Y. Xie, *J. Am. Chem. Soc.* **2014**, *136*, 6826 – 6829.

[13] I. S. Cho, M. Logar, C. H. Lee, L. Cai, F. B. Prinz, X. Zheng, *Nano Lett.* **2014**, *14*, 24 – 31.

[14] Y. Ling, G. Wang, J. Reddy, C. Wang, J. Z. Zhang, Y. Li, *Angew. Chem. Int. Ed.* **2012**, *51*, 4074 – 4079; *Angew. Chem.* **2012**, *124*, 4150 – 4155.

[15] X. Shi, K. Zhang, K. Shin, M. Ma, J. Kwon, I. T. Choi, J. K. Kim, H. K. Kim, D. H. Wang, J. H. Park, *Nano Energy* **2015**, *13*, 182 – 191.

[16] K. Zhang, L. Wang, J. K. Kim, M. Ma, G. Veerappan, C. Lee, K. Kong, H. Lee, J. H. Park, *Energy Environ. Sci.* **2016**, *9*, 499 – 503.

[17] M. Ma, J. K. Kim, K. Zhang, X. Shi, S. J. Kim, J. H. Moon, J. H. Park, *Chem. Mater.* **2014**, *26*, 5592 – 5597.

[18] M. Ma, X. Shi, K. Zhang, S. Kwon, P. Li, J. K. Kim, T. T. Phu, G. Yi, J. H. Park, *Nanoscale* **2016**, *8*, 3474 – 3481.

[19] J. H. Kim, J. W. Jang, H. J. Kang, G. Magesh, J. Y. Kim, J. H. Kim, J. Lee, J. S. Lee, *J. Catal.* **2014**, *317*, 126 – 134.

[20] X. Shi, K. Zhang, J. H. Park, *Int. J. Hydrogen Energy* **2013**, *38*, 12725 – 12732.

[21] P. M. Rao, L. Cai, C. Liu, I. S. Cho, C. H. Lee, J. M. Weisse, P. Yang, X. Zheng, *Nano Lett.* **2014**, *14*, 1099 – 1105.

[22] J. C. Hill, K. Choi, *J. Phys. Chem. C* **2012**, *116*, 7612 – 7620.

[23] Q. Liu, F. Cao, F. Wu, H. Lu, L. Li, *Adv. Mater. Interfaces* **2016**, DOI: 10.1002/admi.201600256.

[24] B. Klahr, S. Gimenez, F. Fabregat-Santiago, T. Hamann, J. Bisquert, *J. Am. Chem. Soc.* **2012**, *134*, 4294 – 4302.

[25] T. Li, J. He, B. Pena, C. P. Berlinguette, *Angew. Chem. Int. Ed.* **2016**, *55*, 1769 – 1772; *Angew. Chem.* **2016**, *128*, 1801 – 1804.

[26] C. Du, X. Yang, M. T. Mayer, H. Hoyt, J. Xie, G. McMahon, G. Bischoping, D. Wang, *Angew. Chem. Int. Ed.* **2013**, *52*, 12692 – 12695; *Angew. Chem.* **2013**, *125*, 12924 – 12927.

[27] F. F. Abdi, L. Han, A. H. M. Smets, M. Zeman, B. Dam, R. van de Krol, *Nat. Commun.* **2013**, *4*, 2195.

[28] G. Wang, Y. Ling, H. Wang, X. Yang, C. Wang, J. Z. Zhang, Y. Li, *Energy Environ. Sci.* **2012**, *5*, 6180 – 6187.

[29] H. Zheng, J. Z. Ou, M. S. Strano, R. B. Kaner, A. Mitchell, K. Kalantar-zadeh, *Adv. Funct. Mater.* **2011**, *21*, 2175 – 2196.

[30] W. Li, P. Da, Y. Zhang, Y. Wang, X. Lin, X. Gong, G. Zheng, *ACS Nano* **2014**, *8*, 11770 – 11777.

[31] G. Liu, J. Han, X. Zhou, L. Huang, F. Zhang, X. Wang, C. Ding, X. Zheng, H. Han, C. Li, *J. Catal.* **2013**, *307*, 148 – 152.

[32] L. Zhang, W. Wang, S. Sun, D. Jiang, *Appl. Catal. B* **2015**, *168–169*, 9 – 13.

Received: May 29, 2016
Revised: July 4, 2016